J. Fluid Mech. (2008), *vol.* 598, *pp.* 1–25. © 2008 Cambridge University Press
doi:10.1017/S0022112007009317 Printed in the United Kingdom

Free-Lagrange simulations of the expansion and jetting collapse of air bubbles in water

C. K. TURANGAN[1]†, A. R. JAMALUDDIN[1]‡, G. J. BALL[2] AND T. G. LEIGHTON[3]¶

[1]School of Engineering Sciences, University of Southampton, Highfield, SO17 1BJ, UK

[2]Atomic Weapons Establishment, Aldermaston, Reading, RG7 4PR, UK

[3]Institute of Sound & Vibration Research, University of Southampton, Highfield, SO17 1BJ, UK

(Received 26 November 2006 and in revised form 20 September 2007)

A free-Lagrange numerical method is implemented to simulate the axisymmetric jetting collapse of air bubbles in water. This is performed for both lithotripter shock-induced collapses of initially stable bubbles, and for free-running cases where the bubble initially contains an overpressure. The code is validated using two test problems (shock-induced bubble collapse using a step shock, and shock–water column interaction) and the results are compared to numerical and experimental results. For the free-running cases, simulations are conducted for a bubble of initial radius 0.3 mm located near a rigid boundary and near an aluminium layer (planar and notched surfaces). The simulations suggest that the boundary and its distance from the bubble influence the flow dynamics, inducing bubble elongation and jetting. They also indicate stress concentration in the aluminium and the likelihood of aluminium deformation associated with bubble collapse events. For the shock-induced collapse, a lithotripter shock, consisting of 56 MPa compressive and −10 MPa tensile waves, interacts with a bubble of initial radius 0.04 mm located in a free field (case 1) and near a rigid boundary (case 2). The interaction of the shock with the bubble causes it to involute and a liquid jet is formed that achieves a velocity exceeding 1.2 km s^{-1} for case 1 and 2.6 km s^{-1} for case 2. The impact of the jet on the downstream wall of the bubble generates a blast wave with peak overpressure exceeding 1 GPa and 1.75 GPa for cases 1 and 2, respectively. The results show that the simulation technique retains sharply resolved gas/liquid interfaces regardless of the degree of geometric deformation, and reveal details of the dynamics of bubble collapse. The effects of compressibility are included for both liquid and gas phases, whereas stress distributions can be predicted within elastic–plastic solid surfaces (both planar and notched) in proximity to cavitation events. There is a movie with the online version of the paper.

1. Introduction

Cavitation bubble collapse has been associated with erosion for nearly 100 years, the main mechanisms being liquid impact as the bubble involutes to form a jet (Plesset & Prosperetti 1977), and the effect of pressure waves which radiate out from the bubble

---

† Present address: Institute of High Performance Computing, Singapore Science Park II, Singapore 117528.

‡ Present address: Romax Technology Limited, Nottingham Science & Technology Park, Nottingham, NG7 2PZ, UK.

¶ Author to whom correspondence should be addressed: tgl@soton.ac.uk

(Rayleigh 1917) and can concentrate as a result of cloud effects (Brunton 1967; Vyas & Preece 1976; Hansson, Kendrinskii & Mørch 1982). Experimental work has progressed to the stage where bubble involutions can be filmed at framing rates of several thousand to 100 million frames per second (Lauterborn 1972; Vogel, Lauterborn & Timm 1989; Field 1991; Ohl *et al.* 1999; Lindau & Lauterborn 2003). The recent experiments performed by Lindau & Lauterborn (2003) are particularly impressive; they observed the bubble jetting, shock wave emissions and the phenomenon of counterjet formation with the observation taken mainly at an oblique angle of 45° as well as from the bottom view through the cuvette wall. Limitations of current numerical models, however, place them some distance from the experimental scenario.

Perhaps the most widely reported numerical method used for treating asymmetrical bubble collapse has been the boundary integral method (BIM) (see for example Blake *et al.* 1997; Fong *et al.* 2006; Klaseboer *et al.* 2006; Turangan *et al.* 2006). However, the model assumes that the liquid phase is incompressible, and that the scalar properties of the gas are spatially uniform. The method is therefore limited in situations in which shock waves play a key role within both phases, such as extracorporeal shock wave lithotripsy (ESWL). Shock wave lithotripsy is a treatment for patients suffering renal, ureteric, salivary duct and gall stone disease where shock waves generated outside the patient's body are used to break the stone to fragments small enough to be passed naturally from the body during urination or dissolved by drugs.

Other numerical methods have also been applied to study cavitation problems. The arbitrary Lagrangian Eulerian (ALE) simulations of Ding & Gracewski (1996) are discussed in § 3. Bourne & Milne (2003) have used a two-dimensional multi-material method to simulate the collapse of cylindrical gas cavities in liquid explosives by strong shock waves. Their simulations incorporate dissociation of the compression-heated cavity gas, and Arrhenius chemistry in the liquid.

In the present work, a free-Lagrange numerical method has been used to simulate axisymmetric bubble collapses, both free-running (i.e. following expansion as a result of an initial gas overpressure), and lithotripter shock-induced collapses of initially stable bubbles. The lithotripter simulations were undertaken to support the design of a device that is currently undergoing clinical trials (Leighton *et al.* 2008). For the free-running cases, new simulation results presented here also include bubble collapses close to metal surfaces in which the stress distribution and the likelihood of deformation within the metal have been predicted. There is interest in these cases because of various experiments to study the mechanisms of material damage associated with cavitation erosion (e.g. Tomita & Shima 1986; Dear & Field 1988*a*; Philipp & Lauterborn 1998).

2. Free-Lagrange numerical method

The *Vucalm* free-Lagrange numerical method introduced in two-dimensional form by Ball (1996) solves the unsteady compressible Euler equations on an unstructured Lagrangian finite-volume mesh. For the work in this paper, the axisymmetric form of the code (Turangan 2004) has been developed and implemented. The flow solver is based on a Godunov approach with nominal second-order accuracy in space, and first-order in time. In contrast to conventional Lagrangian codes, in free-Lagrange schemes the mesh connectivity is allowed to change freely in response to flow deformation. As a consequence, the mesh is immune to tangling, regardless of the degree of flow distortion. Furthermore, the absence of convective inter-cell fluxes results in minimal numerical diffusion of convected flow structures, so that features such as

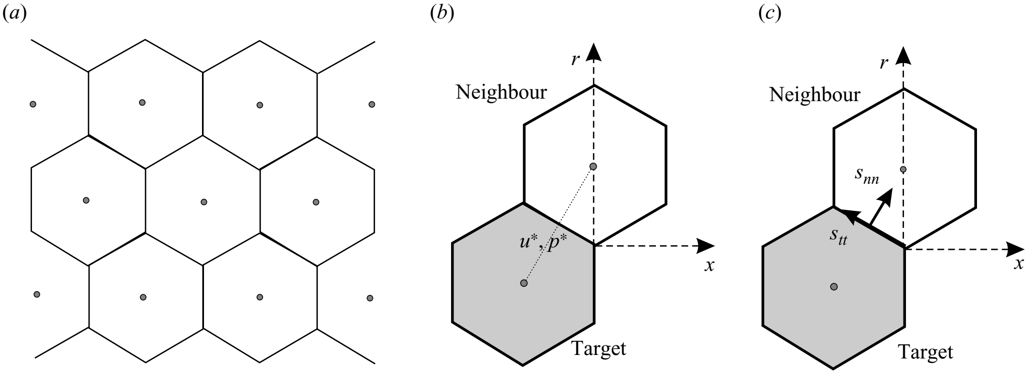

FIGURE 1. (*a*) Typical Voronoi mesh used in *Vucalm* simulations. The dots indicate the cell centre coordinates, and each cell represents a single fluid type. (*b*) Riemann solvers (Godunov-type) compute the numerical fluxes (velocity u^*, pressure p^*) across cell boundaries between the target and neighbour cells to update the values of density ρ, velocities (u, v), pressure p and temperature T. (*c*) If the cell represents material with strength, edge-oriented normal stress (s_{nn}) and shear stress (s_{tt}) are computed to update the deviatoric stresses in the x-direction (s_{xx}) and in the radial r-direction (s_{rr}) (see § 4.2).

material interfaces remain sharply resolved at all times. These characteristics make free-Lagrange schemes well suited to cavitation simulation, in which highly deformed gas/liquid interfaces must be accurately captured.

The computational mesh in *Vucalm* simulations is of Voronoi type (figure 1) (for details see Ball 1996; Howell & Ball 2002). The code makes use of an adaptive mesh technique where each of the coarse fluid cells in the computational domain will automatically be identified and split into two fluid cells of identical properties, but with half the mass and volume ('refinement' procedure). In contrast, the regions with excessive cell density will also be identified, in which adjacent pairs of fluid particles of the same type are merged together ('derefinement' procedure). The *Vucalm* code also uses an interface smoothing algorithm (Howell & Ball 2000), a form of artificial surface tension, to remove the mesh-seeded Richtmyer–Meshkov instability associated with free-Lagrange schemes. The code has been used previously to simulate the shock-induced collapse of cylindrical cavities in water (Ball *et al.* 2000), while the addition of a strength model has facilitated the representation of elastic–plastic solids in high and hypervelocity impact problems (Howell & Ball 2002).

3. Free-Lagrange code validation

Validation of the free-Lagrange code, *Vucalm*, is presented here for multi-phase flow problems in axisymmetric and planar two-dimensional geometries. The test problems are: (*a*) shock-induced collapse of a spherical air bubble by a planar step shock (with validation against the alternative numerical approach of Ding & Gracewski (1996)); and (*b*) the interaction of a shock with a water column (with validation against the experiment of Igra & Takayama (1999)).

3.1. *Shock-induced bubble collapse*

Ding & Gracewski (1996) performed arbitrary Lagrangian Eulerian (ALE) simulations of axisymmetric inviscid compressible flow for air bubble/shock interactions with both weak shocks ($P < 30$ MPa) and strong shocks ($0.5 < P < 2.0$ GPa), where P is the post-shock pressure. The shock wave is of a step shock type. The computational

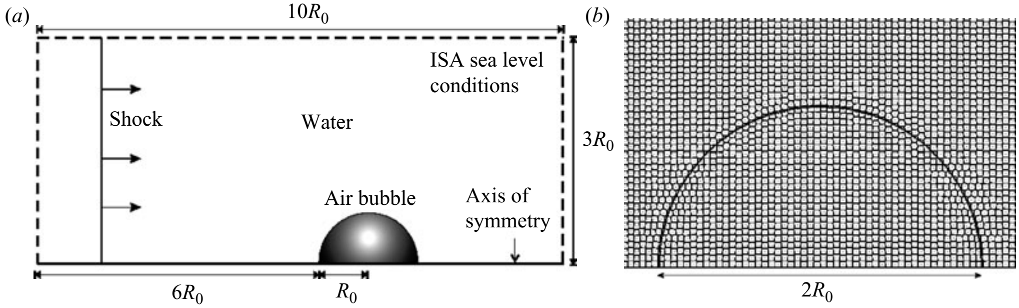

FIGURE 2. (a) The geometry of the axisymmetric Ding & Gracewski problem (figure not to scale). A planar step shock propagates from the left and hits an air bubble with initial radius R_0. (b) Initial computational cell distribution inside and in the vicinity of the bubble.

domain is shown in figure 2. Ding & Gracewski (1996) simulated nine case studies, but owing to space constraints we publish a comparison with only one of those cases, i.e. the case with the initial bubble radius $R_0 = 1$ mm and post-shock pressure $P = 0.528$ GPa. All elapsed times are measured from the first shock/bubble contact.

To discretize the domain, Ding & Gracewski (1996) used 1.28×10^4 non-uniform rectangular cells, in which 64 cells represented the bubble for the case studied here. In our free-Lagrange simulation, approximately 1.9×10^4 polygonal cells are used in the initial unperturbed domain with about 980 cells representing the bubble. From a preliminary study using various numbers of cells (results not shown here), coupled with the use of adaptive mesh 'refinement' and 'derefinement' procedures, we found that this number of cells used in our free-Lagrange simulation is economical and yet enough to capture the jetting collapse and blast wave emission phenomena of shock-induced bubble collapse.

In the free-Lagrange simulation, boundary conditions on the left-hand boundary are initially fixed at post-shock values in order to generate the incoming shock wave. However, from time $t = 1.5$ μs, non-reflecting boundary conditions are applied in order to allow the escape of left-running waves. The upper and right-hand boundaries are non-reflecting at all times. The Tait equation of state (EOS) is used for water, and the ideal gas EOS for air.

Referring to figure 3, as the incident water shock labelled by A strikes the upstream bubble wall, a relatively weak shock is transmitted into the air cavity B, and a strong expansion wave is produced in the water, running upwards and leftwards, C. The particle velocity behind the expansion wave is large, causing the upstream bubble wall to deform, D. Figures 3(a) and 3(b) show Mach contours for the numerical results using ALE and free-Lagrange methods, respectively. Although the two simulations are generally in good agreement, there are minor discrepancies. In particular, the ALE simulation shows localized unphysical behaviour in that the air shock develops a numerical precursor, E, at the bubble boundary which advances ahead of the incident shock, F. Shock resolution is generally better in the free-Lagrange result, particularly within the bubble where compression of the Lagrangian mesh provides a finer mesh resolution.

A distinct water jet moving downstream along the axis of symmetry is formed as a result of the spatially non-uniform deformation of the bubble wall. At $t = 1.6$ μs, the bubble upstream wall that forms the jet tip has penetrated the bubble, isolating a lobe of trapped and highly compressed gas which forms a toroid in three dimensions

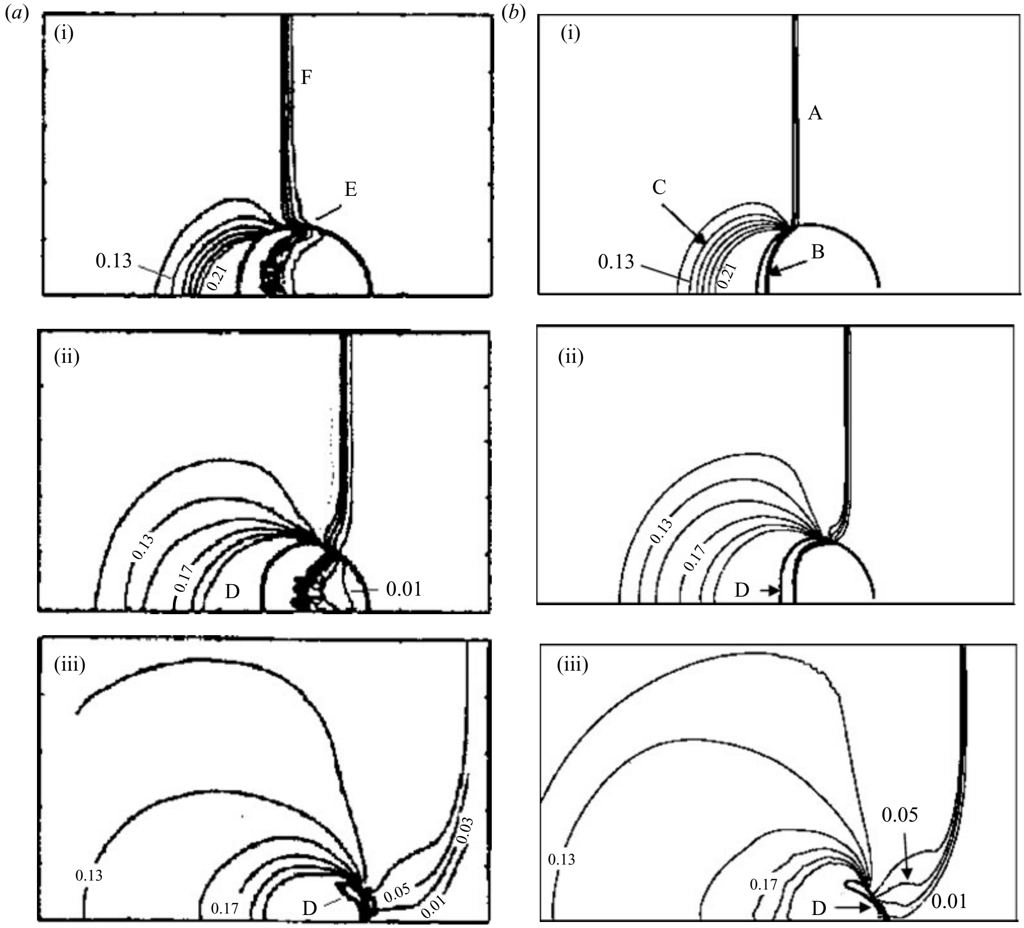

FIGURE 3. Plots of Mach contours. A bubble of $R_0 = 1$ mm is collapsed by a $P = 0.528$ GPa shock. Comparison between (*a*) Ding & Gracewski (1996), and (*b*) *Vucalm*. Labels A–F are described in the text. (i) $t = 0.4$ µs, (ii) 0.8 µs, (iii) 1.6 µs.

(figure 3*b*(iii)). The jet velocity reaches its highest value near the time that the liquid jet impacts on the downstream bubble wall; ALE: 2200 m s^{-1}, free-Lagrange: 2250 m s^{-1}. Ding & Gracewski (1996) reported that their ALE calculation was halted at jet impact owing to deteriorating mesh structure in the bubble, leading to an unacceptably small time step. In our work, a ‘derefinement’ procedure automatically identifies and merges adjacent pairs of fluid particles (of the same fluid type) in regions of excessive mesh density and allows the simulation to run beyond jet impact, while maintaining an acceptable time step (figure 4).

The liquid jet impact on the downstream bubble wall produces an intense blast wave in the surrounding water with an initial peak overpressure exceeding 3.5 GPa. The nature of the simulation confers axis-symmetric symmetry to the predicted blast wave (figure 4*a*). The wave advances relatively slowly to the left because of the high velocity of the liquid jet. At $t = 4.65$ µs (figure 4*b*), the cavity is drawn into a vortex flow, created from the interaction of the high-velocity liquid jet and the relatively static surrounding fluid. Note that the greatest pressure attained during the collapse modelled in figures 3 and 4 occurs in figure 4, after the incompressible code ceases to

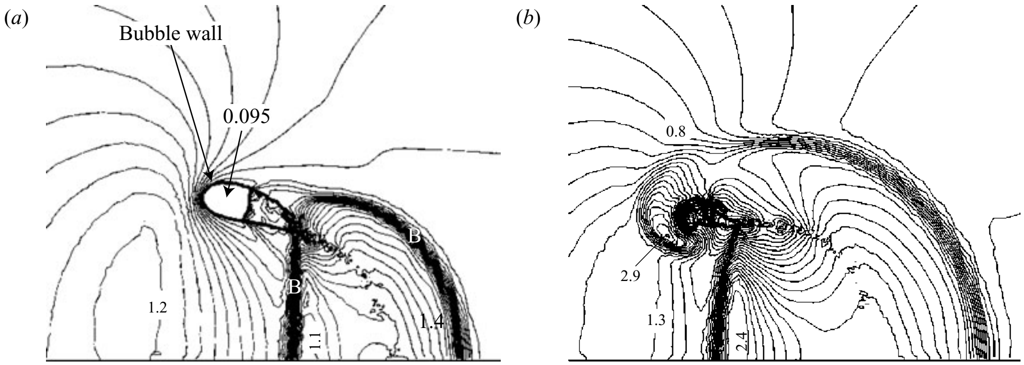

FIGURE 4. Close-up views of the bubble collapse event beyond the high-speed jet impact that occurs at $t = 1.6\,\mu s$. The impact generates an intense blast wave, B, and the bubble turns into a toroid that interacts with the blast wave as seen in (*b*). Contours are pressure: $\Delta P_{water} = 0.1$ GPa, $\Delta P_{air} = 0.050$ GPa. (*a*) $t = 4.58\,\mu s$, (*b*) $4.65\,\mu s$.

be able accurately to predict the pressures in the liquid. This illustrates the importance of using a compressible code when assessing, for example, the acoustic emissions or potential for damage associated with such collapses.

Dear & Field (1988*b*) monitored the collapse of a two-dimensional cavity ($R_0 = 1.5$ mm) in liquid gelatine induced by a 0.26 GPa shock. Their experiment also showed that the high-speed jet forms a cusp-shaped tip when it penetrates the bubble. Although the phenomenon of luminescence is not shown in the free-Lagrange simulation presented here, the highly compressed gas in the bubble fragments produced following the jet impact is likely to luminesce. Such luminescence was observed using image intensification of the jetting collapse of air disks in gel by Dear, Field & Walton (1988) and Bourne & Field (1991).

The interaction of a spherical bubble ($R_0 = 1$ mm) with a 0.528 GPa shock was also simulated by Klaseboer *et al.* (2006) using the boundary integral method (BIM) where the liquid phase was assumed to be incompressible and the shock wave was modelled as a step pulse function incorporated in the Bernoulli equation. Although liquid compressibility effects were overlooked, the simulation captures a similar bubble shape during collapse, and both the collapse time and high-speed jet velocity are in good agreement with those of the ALE results of Ding & Gracewski (1996), and with the free-Lagrange results presented in this paper. However, only the free-Lagrange simulations presented here continue to model beyond the high-speed jet impact.

3.2. *Interaction of an air shock with a water column*

Further validation of the *Vucalm* code was obtained from the experimental interferograms of Igra & Takayama (1999). They investigated the deformation and breakup of a cylindrical water column on shock-wave loading. Figure 5 shows the problem geometry. A cylindrical water column with an initial diameter of 6 mm in air is exposed to a planar shock wave of Mach number $M = 1.47$. The computational domain is discretized using about 3.1×10^4 polygonal cells. For computational convenience, the structure of the cell distribution inside and near the water column in the initial unperturbed domain is as illustrated in figure 5(*b*). However, in the region far from the water column, the cells are rectangular, and the cell density (number of cells per unit area) is less than in the region near the water column.

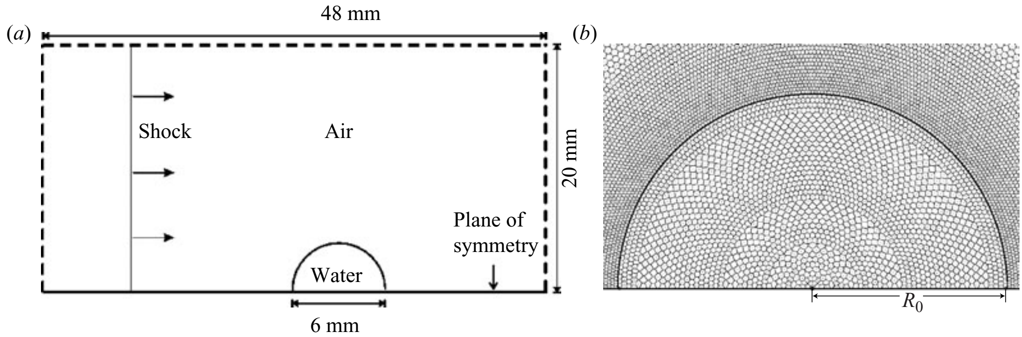

FIGURE 5. (*a*) The geometry of the two-dimensional Igra & Takayama validation problem (figure not to scale). A planar shock propagates from the left and interacts with a water column of 6 mm diameter. (*b*) Initial computational cell distribution inside and in the vicinity of the water column.

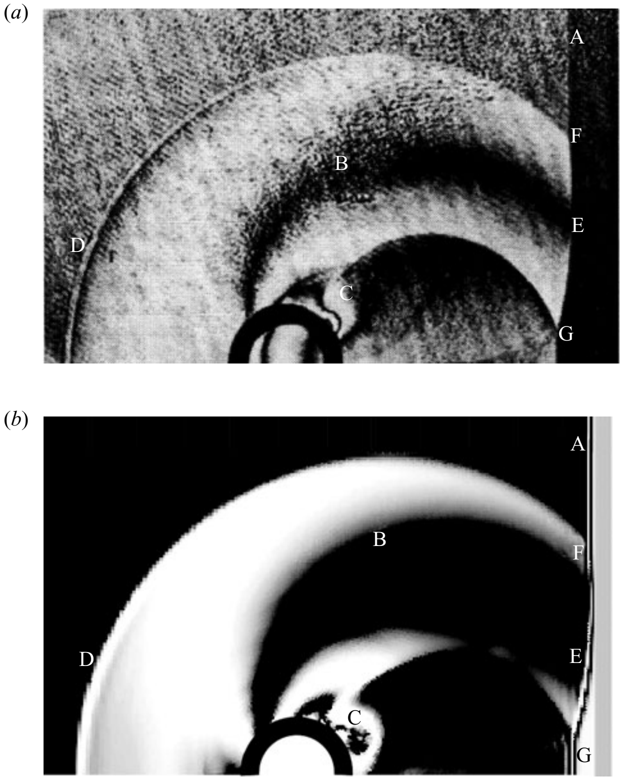

FIGURE 6. Interferogram images. Comparison between (*a*) Igra & Takayama (1999) and (*b*) *Vucalm* for the interaction of a shock wave with a water column, 53 μs after shock impact. Labels A–G are described in the text.

Figure 6(*a*) shows a double exposure holographic interferogram taken from the experiment, while figure 6(*b*) is a numerical interferogram generated from *Vucalm* data. The dark ring seen on the interferogram of figure 6(*a*) indicates the wetted area where the water column contacted a glass surface. The incident shock wave (labelled A) has traversed the water column. The comparison between the two interferogram

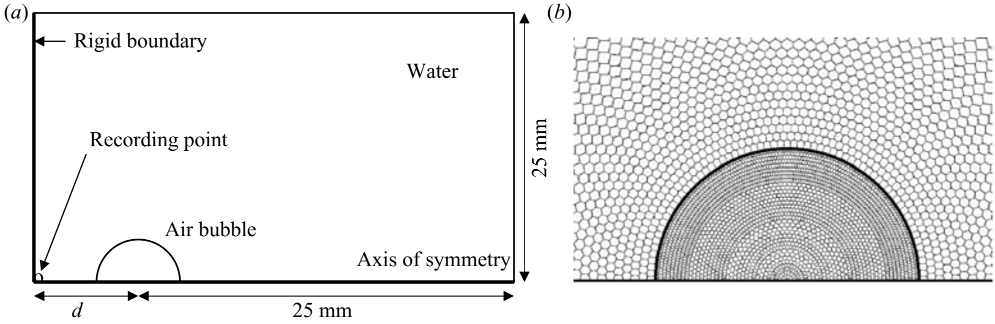

FIGURE 7. (*a*) Schematic of the computational domain of an initially spherical air bubble with $R_0 = 0.3$ mm near a rigid boundary in water (figure not to scale). (*b*) Initial cell distribution inside and in the vicinity of the bubble.

Case	Initial distance d (mm)	R_m (mm)	Stand-off parameter ξ
a	1.44	1.79	0.8
b	2.14	1.80	1.2
c	2.88	1.81	1.6

TABLE 1. Three cases simulated for bubble expansion and collapse near a rigid boundary.

images shows that the general fringe pattern in air agrees well. In particular, it correctly predicts both the vortex structure C on the downstream side of the column, and the form and position of the fringe B that extends from the upstream of the water column to the Mach stem. Furthermore, the predicted location of the reflected wave D, Mach stem E, triple point F and secondary triple point G are in excellent agreement with experiment.

4. Cavitation bubble collapse

4.1. *Collapse near a rigid boundary*

Simulations of single cavitation bubbles near a plane rigid boundary for various stand-off parameters are presented here. The stand-off parameter is defined as $\xi = d/R_m$, where d is the initial distance of the bubble centre from the boundary, and R_m is the bubble maximum radius. The objective is to model the behaviour of a single cavitation bubble which is initially at higher pressure than its surroundings. In practice, such bubbles could be created by laser heating, or by an underwater explosion where the bubbles undergo expansion followed by rapid collapse. Of particular interest are: to observe the conditions in the early stage of the growth phase and those near the maximum volume; and any bubble elongation, high-speed liquid jet formation, jet impact and bubble rebound.

A schematic of the computational domain is shown in figure 7(*a*). The number of cells used to discretize the domain is approximately 8.1×10^3, 8.45×10^3 and 8.7×10^3 for cases *a*, *b* and *c*, respectively, as given in table 1, i.e. based on the stand-off parameter. About 2173 cells of those in the domain are used to represent the bubble. Thus, the larger the stand-off parameter (the larger the initial distance d), the higher the number of cells inside the domain. These numbers of cells were chosen following a grid convergence study, in which three test cases (coarse, intermediate and fine grids)

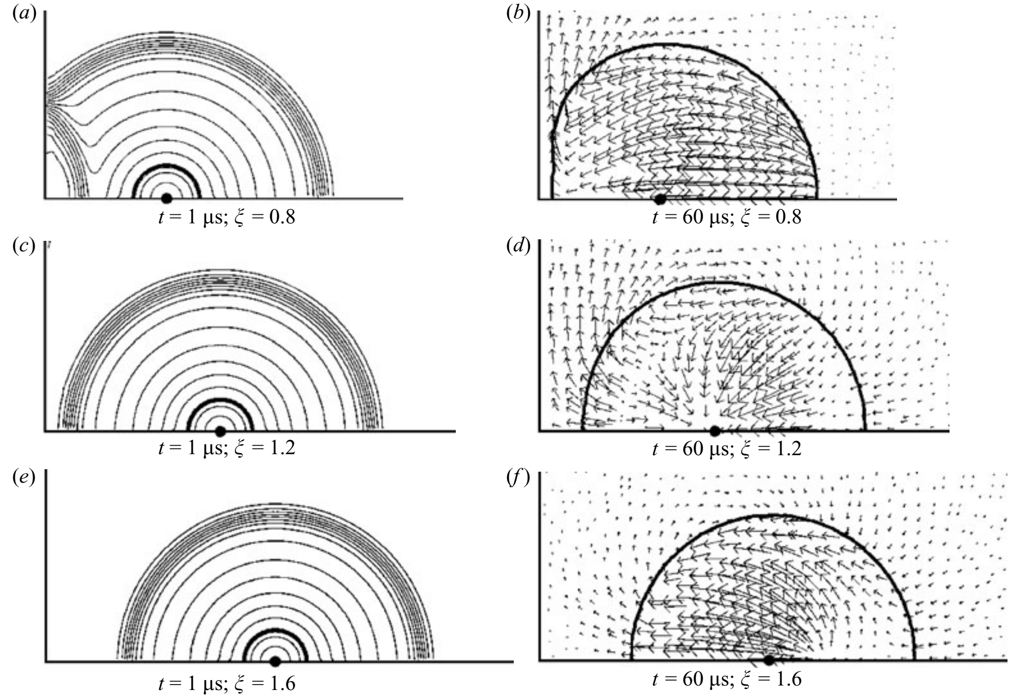

FIGURE 8. Bubbles during expansion with pressure contour plots $\Delta P = 1.5$ MPa (*a*, *c*, *e*), and near maximum volume with velocity vectors plotted (*b*, *d*, *f*) for various ξ. The initial location of the bubble centre is indicated by a black dot; the black solid line represents the bubble wall.

based on the stand-off parameter and conditions of case *b* were run. The number of cells in coarse, intermediate and fine grids was 6.55×10^3, 8.45×10^3 and 11.06×10^3, respectively. The intermediate and fine-grid cases produced similar results, including the plot of bubble volume–time history, which was used as a measure of comparison. Thus, the intermediate grid structure was adopted for case *a* and case *c* simulations.

The initial cell distribution in the domain (figure 7*b*) is arranged in a ‘circular’ structure throughout the domain and in such a way that the cell density is highest in the bubble to accommodate the bubble initial expansion. The cell size representing the water then gradually decreases as the radial distance from the bubble centre increases. This cell arrangement is adopted because the bubble collapse phenomena take place inside and near the bubble.

For computational convenience, the top and right-hand boundaries are reflecting boundaries, and a pressure recording point is located at the intersection of the rigid boundary and the axis of symmetry. The initial pressure and temperature of the bubble, which is modelled to contain air, are 81.06 MPa and 1252 K, respectively. The initial pressure, temperature and density of the water are, respectively, 101.325 kPa, 288.15 K and 1000 kg m^{-3}. The initial radius of the bubble is 0.3 mm. Three cases have been simulated based on the initial distance *d* of the bubble centre from the rigid boundary (table 1). As the bubble is not truly spherical when it reaches its maximum volume, R_m is taken as the radius of a sphere of the same volume.

Following flow initialization, a spherical water shock wave is emitted into the surrounding water and an expansion wave propagates in air towards the centre of the bubble as shown in figure 8(a, c, e). After the air shock passes through the bubble

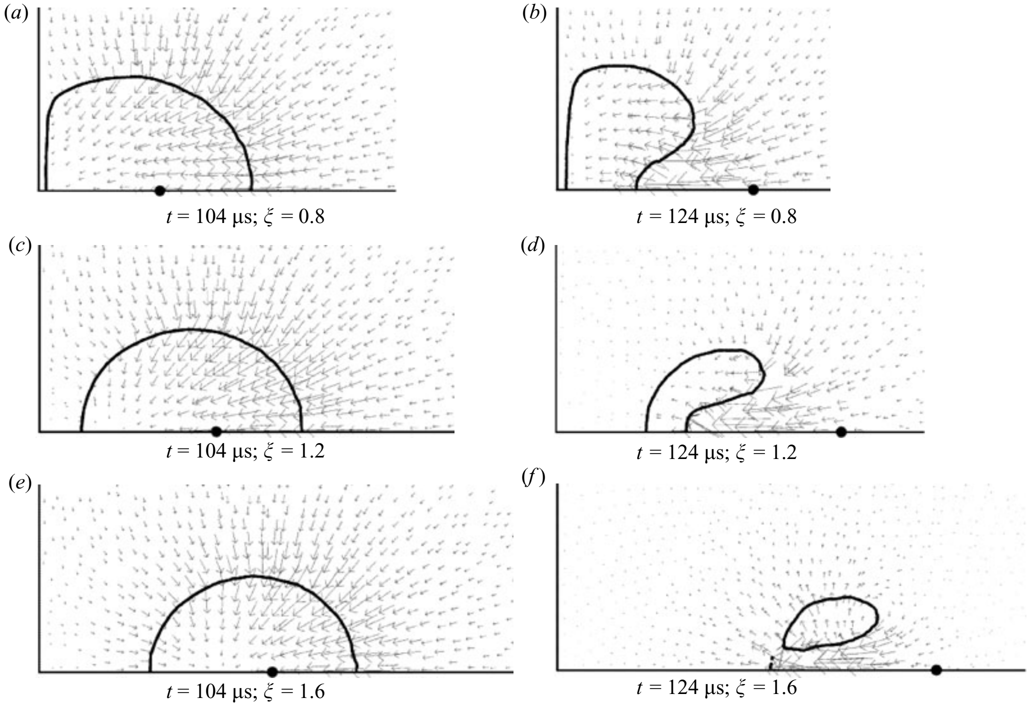

FIGURE 9. Plots of bubble wall and velocity vectors. The bubble elongates (*a*, *c*, *e*) and forms a high-speed jet during the collapse stage (*b*, *d*, *f*).

centre, it generates an expansion wave which propagates outwards away from it. On meeting the bubble wall, this outwardly propagating wave inside the bubble was found to be partly transmitted from the air into the surrounding water, and partly reflected back into the bubble (this event is not shown here for reasons of space). The initial water shock is reflected back into the domain from the rigid boundary on the left-hand side (figure 8*a*). As ξ increases, the magnitude of the resulting pressure peak registered at the recording point decreases, i.e. $P_{max} = 29$ MPa for $\xi = 0.8$, $P_{max} = 18$ MPa for $\xi = 1.2$ and $P_{max} = 13$ MPa for $\xi = 1.6$.

The bubble evolution for three different ξ (table 1) is shown in figures 8 to 10. The velocity vector scaling has been selected in each figure to highlight the flow structure, and is not the same at each stage. In all cases, the bubbles undergo a rapid expansion in the first 20 μs. The presence of the rigid boundary clearly distorts the flow as it redirects the water outwards along the rigid boundary, away from the 'recording point'. For $\xi = 0.8$, the bubble is flattened against the boundary at maximum volume (figure 8*b*), and as ξ increases, the bubbles expand in a more symmetrical pattern. In these simulations, bubble maximum volume is reached at around $t = 60$ μs after the start of bubble growth. At this time, the bubble has over-expanded owing to the inertia of the water. The pressure of the air inside the bubble varies spatially between 0.38 bar and 0.48 bar in all cases, and is well below that of the surrounding water.

The velocity vectors in figure 8(*b*, *d*, *f*) show that at $t = 60$ μs, the water on the right-hand side of the bubble has started to accelerate towards the rigid boundary. This is caused by a local high-pressure region that develops on the right-hand side of the bubble. Meanwhile, the water layer between the bubble and the rigid boundary

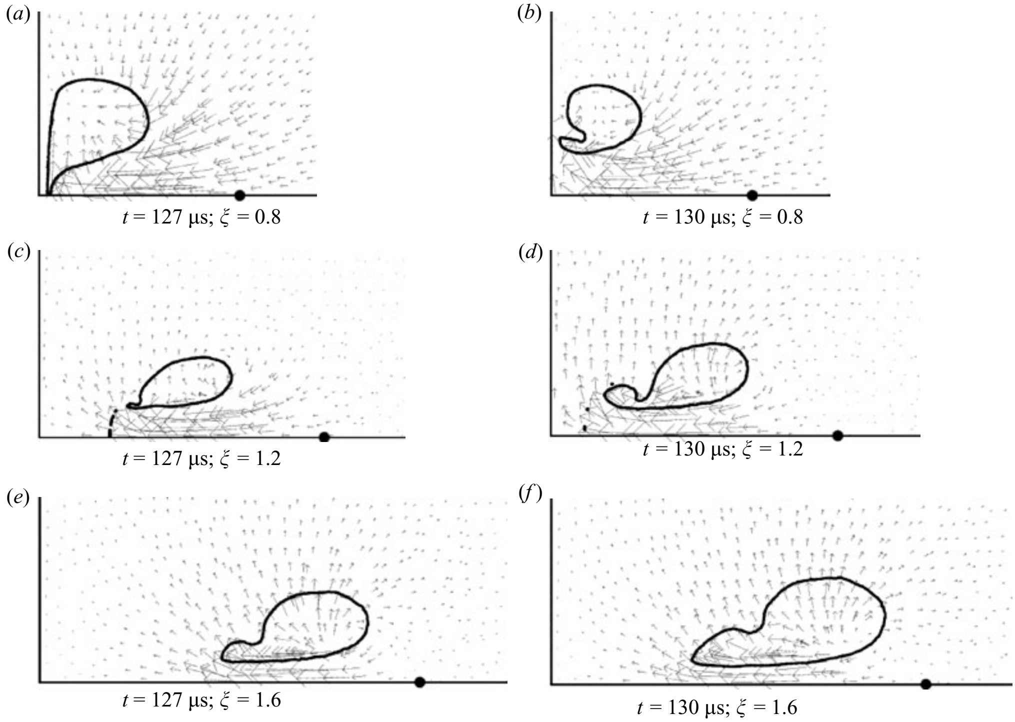

(a) $t = 127$ μs; $\xi = 0.8$
(b) $t = 130$ μs; $\xi = 0.8$
(c) $t = 127$ μs; $\xi = 1.2$
(d) $t = 130$ μs; $\xi = 1.2$
(e) $t = 127$ μs; $\xi = 1.6$
(f) $t = 130$ μs; $\xi = 1.6$

FIGURE 10. The high-speed jet is directed towards the rigid boundary and impacts on the bubble's opposite wall creating a toroidal bubble. After collapse, the bubble rebounds. The microbubbles seen in (*c*) and (*d*) are resolved over several cells, and resemble bubble fragments observed experimentally (see text).

continues to flow towards the wall, and then outwards along the rigid boundary. As the bubble evolution proceeds, the movement of this water layer reverses direction, as seen in figure 9(*c*, *e*).

During the collapse stage, the bubbles elongate. Bubble elongation is a secondary phenomenon of asymmetrical bubble collapse, which has been claimed by Philipp & Lauterborn (1998) to enhance cavitation erosion indirectly. Their experimental observations of the collapse of laser-generated bubbles show that bubble elongation occurs when $1 < \xi < 2.2$. In the current simulations, this event is shown in figure 9(*c*, *e*) where $t = 104\,\mu\text{s}$. To characterize the bubble elongation, an aspect ratio ϕ, given as $\phi = D_x/\sqrt[3]{(6V/\pi)}$, can be calculated, where D_x is the axial diameter of the bubble and V is the bubble volume, $\phi = 1$ for a spherical bubble and $\phi > 1$ on elongation. At $t = 104\,\mu\text{s}$, the aspect ratios are 0.907, 1.0497 and 1.0505 for $\xi = 0.8$, $\xi = 1.2$ and $\xi = 1.6$, respectively.

The right-hand bubble wall accelerates and later involutes to form a high-speed liquid jet, which penetrates the bubble in the direction of the rigid boundary. Figure 9(*b*, *d*, *f*) shows high-speed jets penetrating the bubbles at $t = 124\,\mu\text{s}$. The jet eventually impacts on the opposite bubble wall (liquid–liquid impact) and the event emits a blast wave. The maximum liquid jet velocity is found to increase with increasing ξ, the jet velocities are $168\,\text{m}\,\text{s}^{-1}$, $198\,\text{m}\,\text{s}^{-1}$ and $224\,\text{m}\,\text{s}^{-1}$ for $\xi = 0.8$, $\xi = 1.2$ and $\xi = 1.6$, respectively. Immediately prior to impact, the jet tip is slowed down by the trapped air layer between the tip and the opposite bubble wall. The simulations suggest that, on impact, some of the trapped air is encapsulated in micro-bubbles. These micro-bubbles, shown in figure 10(*c*) where bubble fragments are seen as dark specks located below and to the left of the main bubble after jet impact, are resolved using several cells. They are eventually scattered by the toroidal flow created by the momentum of the high-speed jet and their size decreases as they move away from the axis of symmetry. Although such micro-bubbles were also observed experimentally by Tomita & Shima (1986), simulations may require much finer cells than are used in figure 10(*c*) to represent their size, evolution and existence.

Following the jet impact, the bubbles turn into toroids and the flow creates a ring vortex (figure 10*b*–*f*). The momentum of the jet causes the bubbles to migrate towards the rigid boundary. The bubble wall continues to contract until the pressure inside is much higher than that of the surrounding water, which initiates bubble rebound (figure 10*d*, *f*). The combined effect of both the high-speed liquid-jet impact and the bubble rebound are believed to be associated with surface erosion (Shima 1997).

4.2. *Collapse near an aluminium layer*

Various experimental investigations have explored the growth and collapse of spark- or laser-generated bubbles in the vicinity of a strong material to study the mechanism of cavitation erosion (Philipp & Lauterborn 1998; Tomita & Shima 1986). Aluminium is the most commonly used boundary specimen. Because of aluminium's low yield strength, it is easier to observe the indentation caused by the collapse of bubbles on aluminium than on other materials such as steel or indium. Nevertheless, it is reported that around 100 laser shots are normally required to produce significant plastic deformation on an aluminium surface (Philipp & Lauterborn 1998).

In the present work, the simulations are limited to single bubble collapse events close to aluminium surfaces. The aims are to observe the stress loading in planar and 'notched' aluminium targets during the initial shock loading and blast loading from the jet impact at which the stresses are maximum. The behaviour of a strong material under loading is represented using an elastic–perfectly plastic material model, implemented using the method of radial return (Howell & Ball 2002).

To assess the conditions in which the aluminium model deforms, the yield criterion in axisymmetric geometry given by the inequality

$$s_{xx}^2 + s_{yy}^2 + s_{\theta\theta}^2 + 2s_{xy}^2 \leqslant \tfrac{2}{3}(Y_0)^2 \tag{4.1}$$

is considered, where s_{xx} and s_{yy} are the deviatoric normal stresses in the x- and y-directions, respectively, $s_{\theta\theta}$ is the hoop stress, s_{xy} is the deviatoric shear stress and Y_0 is the yield strength of the corresponding material. The deviatoric stress is the stress associated with the resistance of the material to shear distortion. This inequality is the von Mises yield condition stated in axisymmetric fixed deviatoric space (Wilkins 1999). In the scheme employed here, the quantity $\Im = 2J_2 = s_{xx}^2 + s_{yy}^2 + s_{\theta\theta}^2 + 2s_{xy}^2$ is calculated to determine the elastic–plastic yield where J_2 refers to the second invariant of stress.

The computational domains are illustrated in figure 11. The initial number of computational cells inside the domain was 1.44×10^4, of which about 5.6×10^3 were assigned as aluminium and the rest as water and air for the bubble. The cell distribution is similar to that shown in figure 7(*b*). The initial conditions of the water and bubble and the initial bubble radius are the same as in the rigid boundary cases (§ 4.1). The maximum radius is $R_m \approx 1.8$ mm and $\xi = 0.8$. For the aluminium, which is represented by the Osborne equation of state (Howell & Ball 2002), the initial conditions are: ambient pressure $p = 101.325$ kPa, density $\rho = 2785\,\mathrm{kg\,m^{-3}}$ and specific internal energy $\epsilon = 15.84\,\mathrm{J\,kg^{-1}}$. The shear modulus, μ, and yield strength, Y_0,

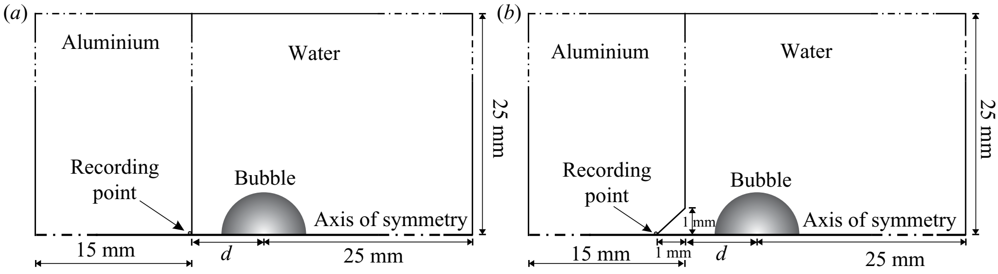

FIGURE 11. Schematic of the computational domains for simulations of an initially spherical air bubble with $R_0 = 0.3$ mm that expands and collapses near an aluminium layer in water. $d = 1.44$ mm (figure not to scale). (*a*) Planar aluminium; (*b*) notched aluminium.

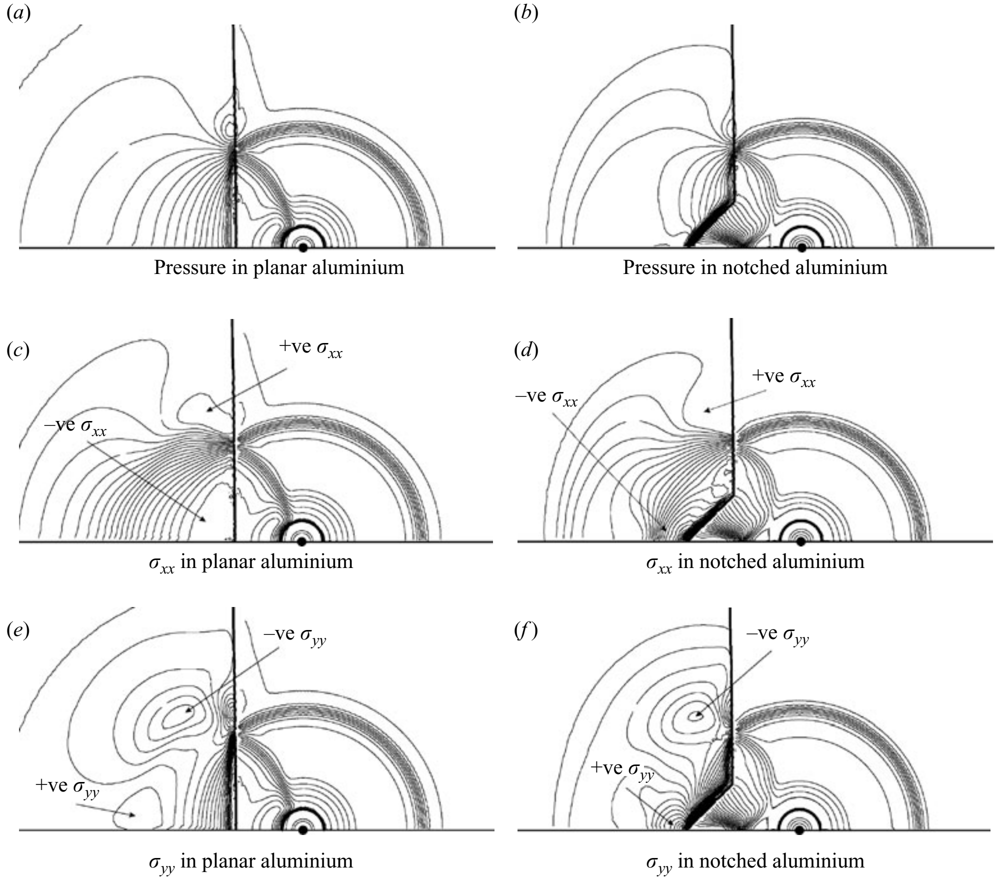

Pressure in planar aluminium

Pressure in notched aluminium

σ_{xx} in planar aluminium

σ_{xx} in notched aluminium

σ_{yy} in planar aluminium

σ_{yy} in notched aluminium

FIGURE 12. Plots of pressure contours in water, bubble and aluminium with pressure interval $\Delta p = 1$ MPa, and stresses σ_{xx} and σ_{yy} in aluminium in early bubble expansion ($t = 1.5$ μs).

of the aluminium are 26.5 GPa and 0.3 GPa, respectively. Thus, to undergo yielding, the value of $\mathfrak{I}$ of the aluminium should exceed 6×10^{16} Pa^2.

Following the start of bubble growth, the shock front that impacts on the aluminium surface is partly transmitted into the aluminium and is partly reflected back into the surrounding water. As shown by pressure contours in figure 12(*a*, *b*), the wave

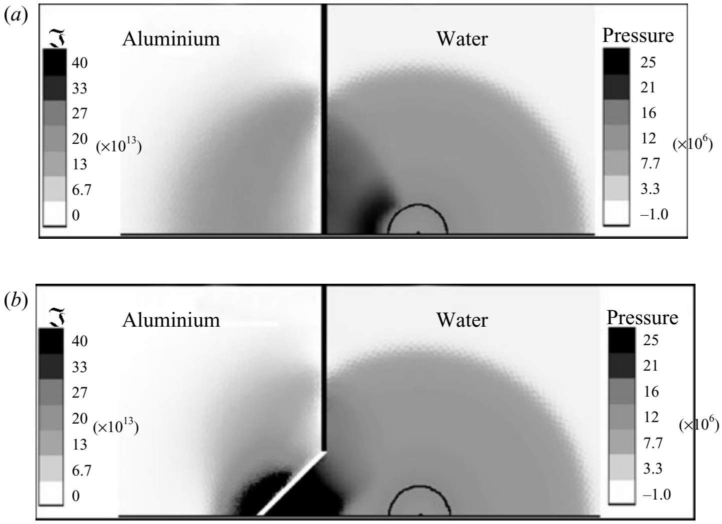

FIGURE 13. Shading plot of quantity $\Im$ in aluminium (in Pa^2) and pressure (in Pa) elsewhere at $t = 1.5\,\mu\mathrm{s}$. (*a*) Planar boundary, (*b*) notched boundary.

propagation inside the aluminium is faster than in the water. Figure 12(*c*–*f*) depicts the plots of total stress contours in the x- and y-directions in aluminium (σ_{xx} and σ_{yy}, where e.g. $\sigma_{xx} = -p + s_{xx}$) at $t = 1.5\,\mu\mathrm{s}$ for the two cases simulated here. The geometry of the notch causes a shock focusing in the water trapped in the notch that gives rise to steep pressure and total stresses (σ_{xx} and σ_{yy}) gradients inside the aluminium along the notch. This also results in the concentration of negative σ_{xx} (compression) and positive σ_{yy} (tension) in small regions around the notch tip, as opposed to the planar aluminium case where the associated regions are wider (figure 12*c*–*f*). In both cases, however, the shock loading resulting from the flow initialization is not strong enough to produce plastic deformation in the aluminium.

In figure 13, the shading plots of $\Im$ in aluminium for the two cases at $t = 1.5\,\mu\mathrm{s}$ are compared. In the planar case, moderately high values of $\Im$ of up to $1.97 \times 10^{14}\,\mathrm{Pa}^2$ are produced behind the initial shock inside the aluminium layer. In the notch case, a stress concentration at the tip of the notch creates a localized high $\Im$ region with maximum value of $8.4 \times 10^{14}\,\mathrm{Pa}^2$, which correlates with a high-pressure region in the water inside the notch. The region in the aluminium with the high value of $\Im$ indicates the location with the closest condition to yield. The phenomenon of stress concentration resulting from shock focusing during bubble collapse has been investigated experimentally by Dear & Field (1988*a*).

The evolution of the bubbles in both cases is similar to the rigid boundary cases previously described. Maximum jet velocities are $168\,\mathrm{m\,s^{-1}}$ for the planar case and $158\,\mathrm{m\,s^{-1}}$ for the notched case. For the notched case, the jet impact is slightly delayed by about $0.5\,\mu\mathrm{s}$ because the left-hand bubble wall is free to deform leftward into the notch. The late stage of the bubble evolution is depicted in figure 14. Momentum supply by the jet creates a stagnation point on the aluminium surface near the axis of symmetry, where upon impact the flow is redirected outwards away from the axis of symmetry (figure 14*a*, *b*).

Figure 15 shows the distribution of $\Im$ induced by the blast wave following the jet impact. For clarity, the dynamic ranges of the greyscales used in figure 15 differ from those used for figure 13. The region with high $\Im$ value inside the notched aluminium

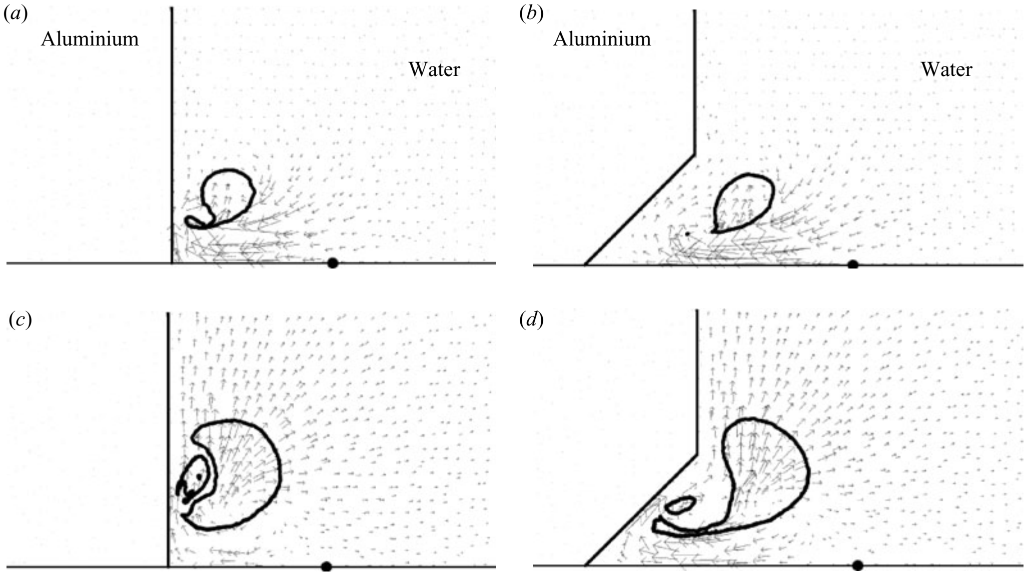

FIGURE 14. Late-stage bubble evolution near planar (*a*, *c*) and notched (*b*, *d*) aluminium surfaces. Parts of the bubble fragment to form micro-bubbles following the jet impact. Here these micro-bubbles are resolved using several to tens of cells depending on their size. (*a*) $t = 134\,\mu s$, (*b*) 134 μs (*c*) 150 μs, (*d*) 150 μs.

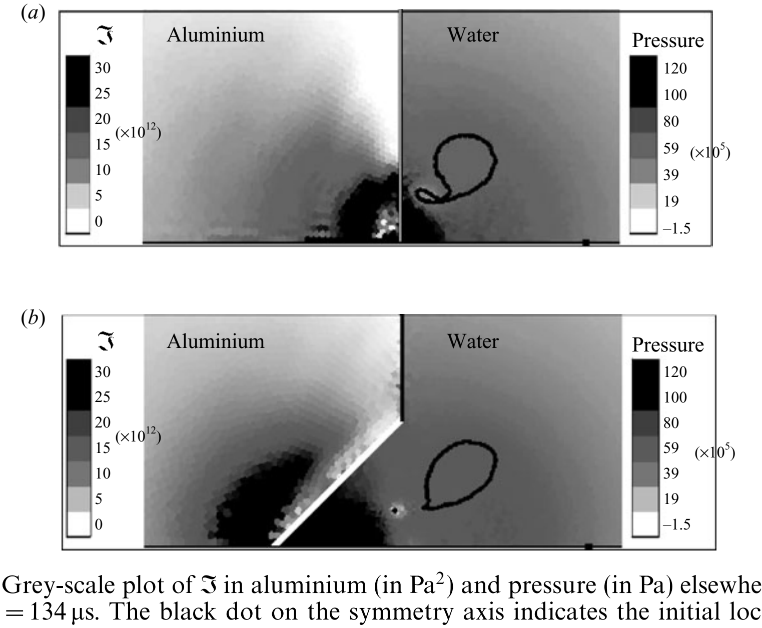

FIGURE 15. Grey-scale plot of $\Im$ in aluminium (in Pa^2) and pressure (in Pa) elsewhere following jet impact, $t = 134\,\mu s$. The black dot on the symmetry axis indicates the initial location of the bubble centre. (*a*) Planar boundary, (*b*) notched boundary.

is wider than that in the planar aluminium. In the planar case, however, a region of high $\Im$ is also obvious near the bubble roll-up. This location forms a circular region of high $\Im$, which may correspond to the circular indentation pattern observed experimentally (Philipp & Lauterborn 1998). For the notched aluminium case, the

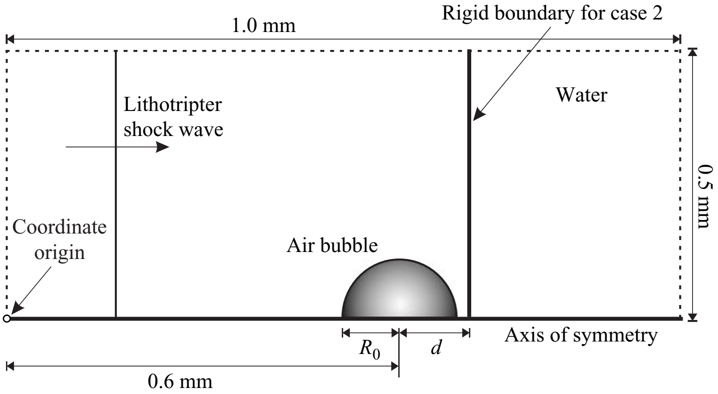

FIGURE 16. Schematic of the lithotripter shock wave–bubble interaction problems (not to scale). The shock propagates from the left towards the bubble with initial radius R_0. For case 1, the bubble is in free field, and for case 2, the bubble is located at a distance d from a rigid boundary. The domain is initially filled with a total of 4×10^4 cells for the free-field case and 3.5×10^4 cells for the rigid-boundary case, respectively. The cell distribution is similar to that in figure 2(*b*), but with a finer mesh in the water surrounding the bubble. A typical animation for a lithotripter-induced bubble collapse (based on the free field case modelled by Jamaluddin *et al.* 2002) is available with the online version of this paper.

location of high $\Im$ concentrates around the tip of the notch as shown in figure 15(*b*). Although in these simulations the aluminium layers are still in the elastic regime, locations of high $\Im$ are likely to experience plastic deformation should the impulse pressure produced by the jet impact and the shock wave of the rebound be more powerful.

5. Lithotripter shock-induced collapse of an initially stable bubble

Extracorporeal Shock Wave Lithotripsy is the clinical procedure by which thousands of shock waves, emitted at roughly one per second, are focused onto kidney stones in order to break them up to a size small enough to be passed naturally from the body, or dissolved with drugs. The incident shock wave interacts with the stone in many ways, including spallation and cavitation (Zeman *et al.* 1990; Kuwahara *et al.* 1991; Coleman *et al.* 1992; Lush *et al.* 1992; Philipp *et al.* 1993; Tomita *et al.* 1994; Sapozhnikov *et al.* 2001; Bailey *et al.* 2003; Leighton 2004).

Here, we consider two problems involving the interaction of a single spherical air bubble, immersed in water, with a lithotripter shock wave (figure 16). Case 1 comprises a bubble in free field, while in case 2 the bubble is adjacent to a rigid boundary, positioned at distance d from the initial centre of the air bubble. The initial air bubble radius, R_0, is 0.04 mm (Cunningham *et al.* 2001), which was chosen to be typical of a secondary stable bubble, i.e. a bubble which has been formed as a result of the interaction of a preceding lithotripter pulse with a cavitation nucleus, and which has reached a state of mechanical equilibrium with the surrounding fluid. In case 2, the distance of the initial bubble centre to the boundary, d, is 0.0425 mm.

The lithotripter pulse is introduced by mapping the pulse profile within the computational domain and a corresponding time-dependent pressure boundary condition is imposed on the left-hand boundary. An idealized planar lithotripter pulse (Church 1989) with $P^+ = 56\,\text{MPa}$ and $P^- = -10\,\text{MPa}$ (figure 17) is set to propagate

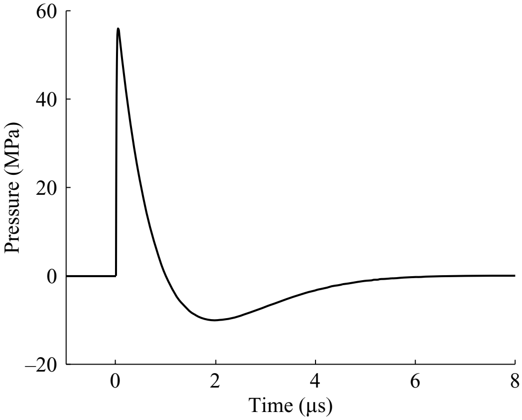

FIGURE 17. The idealized profile of a lithotripter pulse. The compressive wave pressure is $P^+ = 56$ MPa and tensile wave pressure is $P^- = -10$ MPa.

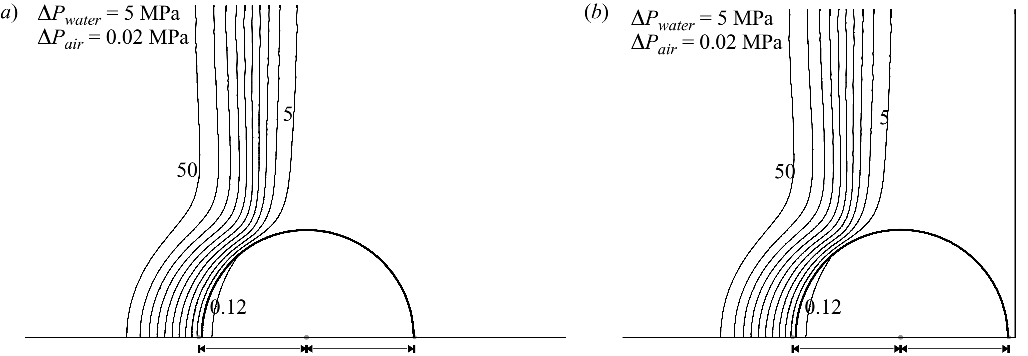

FIGURE 18. (*a*) Free field, case 1; (*b*) near rigid boundary, case 2. Time $t = 0.0247$ μs after shock impact against the upstream wall of the bubble. Horizontal arrows indicate the initial position and size of bubble: the two arrows meet at the initial postion of the bubble centre, and extend a distance R_0 in each direction. The thicker line indicates the position of the bubble wall at $t = 0.0247$ μs. The symbols ΔP_{water} and ΔP_{air} indicate the increments between contours in the water and air, respectively. Units are in MPa.

through the water from left to right. A non-reflecting boundary condition is applied to the top boundary. All elapsed times are measured from the first shock/bubble impact.

Figure 18 shows the pressure field 0.0247 μs after shock impact. As a result of the profound acoustic impedance mismatch, a relatively weak shock is transmitted into the air bubble when the lithotripter shock meets the left-hand bubble wall, whilst a strong expansion fan is produced in the water, running leftwards and upwards. The interaction between the shock and expansion waves originating at the bubble wall results in weakening and curvature of the incident shock, whilst the high particle velocity behind the shock causes the bubble wall to deform to the right. At $t = 0.0919$ μs, the incident shock has traversed the full bubble width (figure 19).

In case 2 (figure 19*b*), the incident shock is reflected off the nearby rigid boundary and further interacts with the expansion wave and the collapsing bubble, weakening the former. In both cases, the air shock propagates more slowly and decouples from the incident shock. Figure 20 shows the motion and velocity of the bubble wall. The graph shows two sets of curves, each set representing the upstream and downstream

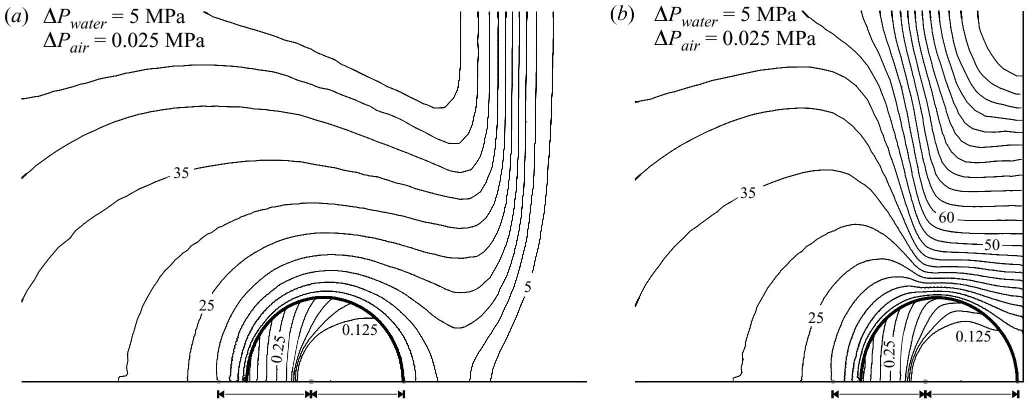

FIGURE 19. (*a*) Free field, case 1; (*b*) Near rigid boundary, case 2. Time $t = 0.0919\,\mu\text{s}$ after shock impact. The incident shock has traversed the full bubble width. In case 2, the incident shock has been reflected from the rigid boundary. In each frame two arrows, each of length R_0, meet at the initial position of the bubble centre. The thick line indicates the bubble wall at $t = 0.0919\,\mu\text{s}$.

wall in cases 1 and 2. Both sets of curves in figure 20(*a*), for cases 1 and 2 show similar trends in that the upstream wall undergoes much more rapid deformation than the downstream wall. The downstream bubble wall remains stationary up to $t \approx 0.08\,\mu\text{s}$ for case 1 and $t \approx 0.15\,\mu\text{s}$ for case 2.

The initially weak air shock propagating within the bubble strengthens owing to the focusing effect arising from the curvature of the bubble interface (figure 19). The shock within the bubble converges as it moves towards the bubble downstream wall. The intricate shape of the air shock is a consequence of the geometry of the bubble wall (which confines the shock), and the variation of the geometry with time. Moreover, the spatially non-uniform deformation of the bubble wall yields a higher water velocity on the bubble centreline. This, in turn, generates additional compression waves in the air near the upstream bubble wall, which further strengthens the air shock.

After the incident shock has swept over the bubble, the whole bubble is enclosed by higher pressure and collapses from all sides, yet asymmetrically owing to the non-uniform momentum transfer and pressure distribution. In case 2, interaction between the water shock reflected from the rigid wall, and the expansion wave increases the amplitude of the high-pressure region adjacent to the upstream bubble wall (figure 21). The impact of the reflected shock on the top side of the bubble also induces the contraction of the bubble wall. Consequently, at $t = 0.1675\,\mu\text{s}$, the top interface of the collapsing bubble in case 2 is more flattened than that in case 1.

At this stage, the bubble undergoes rapid deformation, with the formation of a liquid jet running to the right along the symmetry axis. This occurs in both cases. However, for the bubble near a rigid boundary, the jet tip has a concave curvature (figure 21*b*). It is postulated that this results from recirculating flow at the tip of the jet, induced near the upstream bubble wall by the interaction of the reflected incident shock with the strong expansion wave originating from the bubble wall. Furthermore, as the jet deforms the upstream bubble wall, compression waves are produced in the air. In case 2, the intense high-pressure region close to the tip of the jet (max 750 MPa) induces a secondary air shock with magnitude of over 90 MPa, which propagates to the right inside the bubble.

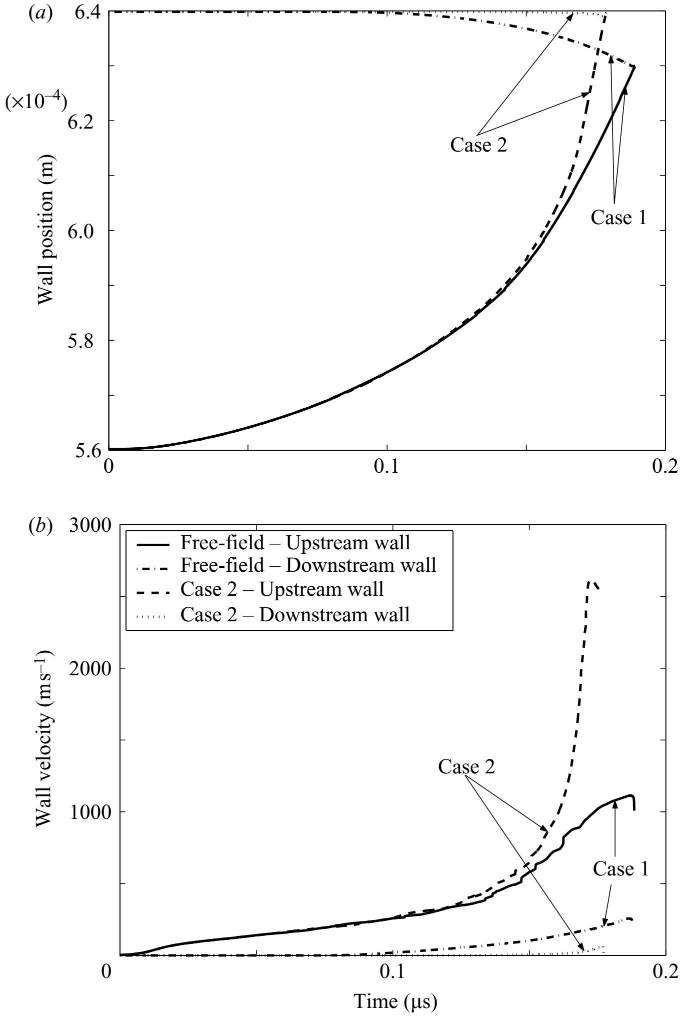

FIGURE 20. (*a*) Upstream and downstream wall position variation with time for cases 1 and 2. The initial centre of the bubble lies at 0.6 mm from the origin (see figure 16) and wall positions are quoted as the on-axis distance from that origin. (*b*) Corresponding wall velocity time history for cases 1 and 2.

The jet impact for the two cases occurs at the point where the two lines representing the upstream and downstream walls in figure 20(*a*) meet, at $t = 0.1890\,\mu\text{s}$ and $t = 0.1789\,\mu\text{s}$ for cases 1 and 2, respectively. Although the downstream wall in case 1 has a greater acceleration than in case 2, the higher jet velocity and collapse rate in the latter means that the jet impact occurs earlier in time in case 2 compared to case 1.

The liquid jet impact isolates a lobe of trapped and highly compressed gas which forms a toroid in three dimensions (figure 22). The geometry of the bubble on impact differs between cases: in case 2 it is more elongated and has a relatively sharper jet compared to case 1, where the liquid jet is much broader. The jet accelerates as it pierces the bubble, reaching a maximum of over $1200\,\text{m}\,\text{s}^{-1}$ and $2600\,\text{m}\,\text{s}^{-1}$ for cases 1 and 2, respectively. Figure 20(*b*) shows that, after $t = 0.1\,\mu\text{s}$, the jet experiences much higher acceleration in case 2. This increased acceleration correlates with the

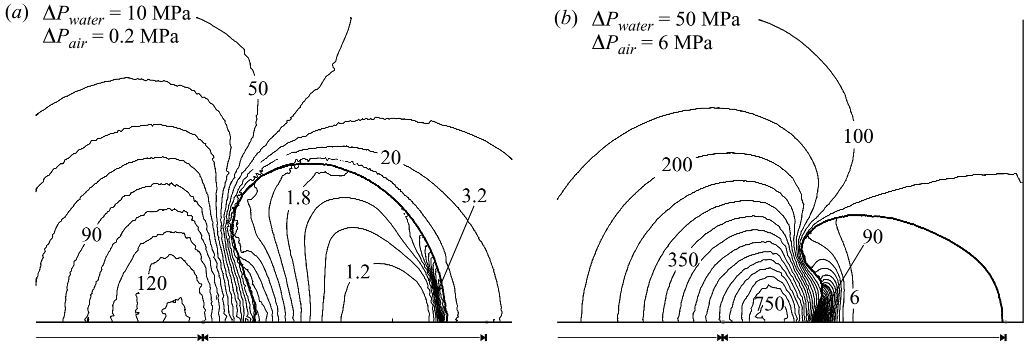

FIGURE 21. (*a*) Free field, case 1; (*b*) near rigid boundary, case 2. Time $t = 0.1675\,\mu$s after the shock impacts on the bubble upstream wall, inducing a formation of a high-speed jet from the involution of the bubble upstream wall when the shock interacts with the bubble. For the bubble near a rigid boundary, the jet tip has a distinct concave curvature and the bubble wall at the tip meets the axis of symmetry at 90°. A portion of the arrow pair from figure 18 is visible.

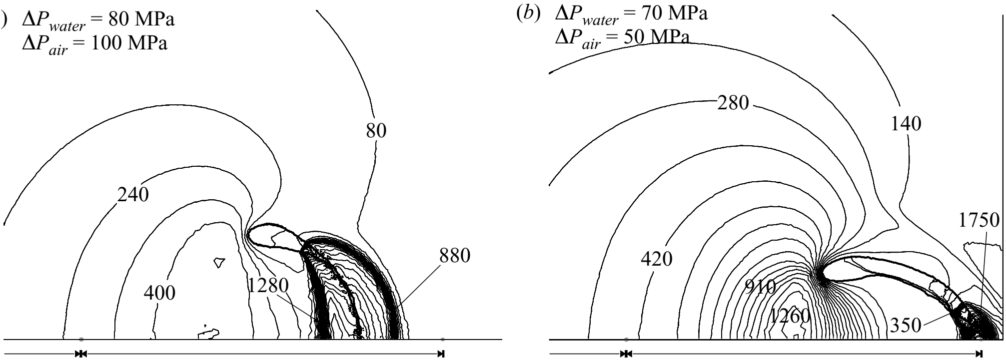

FIGURE 22. (*a*) Case 1, $t = 0.191\,\mu$s; (*b*) case 2, $t = 0.179\,\mu$s. The liquid jet pierces through the bubble and impacts on the downstream wall, generating an intense blast wave into the surrounding water. The bubble in case 2 is more elongated in the horizontal direction than that in case 1 owing to the disturbance of the flow field caused by the presence of the rigid boundary. A portion of the arrow pair from figure 18 is visible.

development of the enhanced high pressure that reaches 1.26 GPa in the region near the throat formed by the bubble torus as seen in figure 22(*b*).

On impact, the jet generates a blast wave in the surrounding water (figure 22). It also leads to the creation of bubble fragments, originating from the air layer trapped between the jet tip and the downstream interface prior to impact. Such tiny isolated islands of gas may coalesce (Leighton *et al.* 2000) with the main cavity as the flow evolves or during the subsequent expansion phase, or act as nuclei for further cavitation events. The interaction of these nuclei with the tensile part of the lithotripter shock wave will cause them to expand and collapse, either spherically or asymmetrically, depending on the nature of the flow around the bubble and the degree of influence of the nearby solid boundary. These bubble fragments could also be collapsed by shock waves emitted from the collapse of neighbouring bubbles.

The maximum effect of the blast wave is localized at the point of liquid–liquid impact, and the peak overpressure decays rapidly with distance from the jet impact

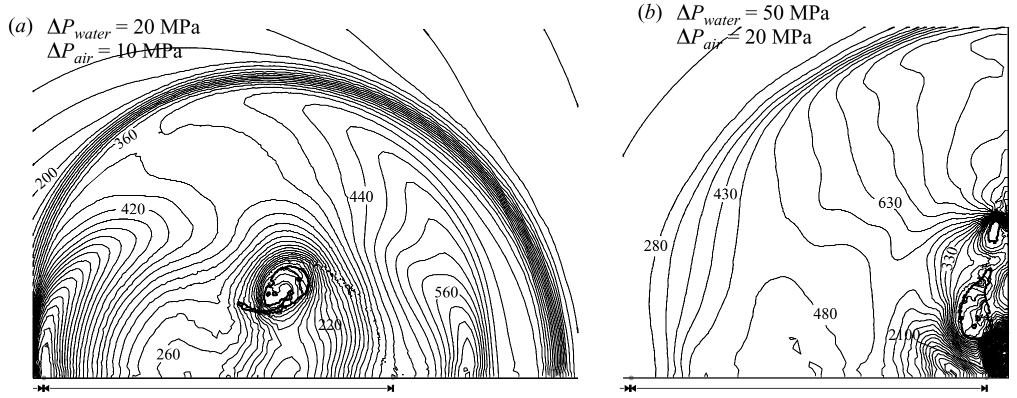

FIGURE 23. (a) Case 1, $t = 0.2025\,\mu$s; (b) case 2, $t = 0.1938\,\mu$s. The blast wave propagates into the surrounding fluid while the cavity is drawn into the vortex core. In case 2, the cavity remains close to the boundary. The blast velocity is in excess of $2000\,\mathrm{m\,s^{-1}}$. The cell containing the maximum pressure (2100 MPa) is indicated by an arrow. A portion of the arrow pair from figure 18 is visible.

point. The peak overpressure exceeds 1 GPa in case 1 and over 1.75 GPa in case 2 owing to the higher jet velocity and more violent collapse.

In case 2, the blast wave impacts on the rigid boundary and is reflected back into the surrounding fluid. Part of this wave interacts with the remaining cavity (figure 23*b*). In addition, the flow is also redirected outwards along the rigid boundary, which brings the bubble and its fragments even closer to the boundary. As a result of the high velocity of the jet fluid, the blast wave advances relatively slowly to the left below the bubble. Consequently, the blast front is asymmetric. Furthermore, the interaction between the high-momentum liquid jet and the downstream low-momentum water produces a strong vortex flow. In figure 23(*a*) (case 1), the air cavity is drawn into the vortex core, while the blast wave continues to propagate outwards from the bubble. The momentum supply of the liquid jet creates a stagnation point, resulting in a high-pressure region near the boundary.

Figure 24 shows the time history of the bubble volume ratio. Both cases show a similar trend, in that the volume reduces with time from shock–bubble impact until the first minimum at $t = 0.1937\,\mu$s and $t = 0.1845\,\mu$s for cases 1 and 2, respectively (see inset of figure 24). The time of minimum volume does not coincide with the time of liquid jet impact (case 1: $t = 0.1889\,\mu$s, case 2: $t = 0.1787\,\mu$s, from figure 20*a*). The volume of the remaining cavity continues to decrease beyond the point of jet impact, although with a slower rate as the higher pressure of the compressed gas in the bubble decelerates the movement of the bubble wall. The two curves follow a very similar path up to about $t = 0.1\,\mu$s. After this time, the two lines begin to diverge, because the reduction in bubble volume in case 2 is higher than in the free-field problem. Figure 20(*b*) shows that the time $t = 0.1\,\mu$s also corresponds to the moment when the upstream wall velocities in the two cases diverge.

In both cases, at the point of minimum volume, the internal pressure greatly exceeds that of the surrounding water, and therefore the bubble begins to expand. It is well-known that, on a gross scale, this expansion leads to a prolonged period where the bubble expands to many times its original size. This phase persists for tens of microseconds or longer before the bubble undergoes a second major collapse (Church 1989). This time scale is longer than that for which the free-Lagrange code

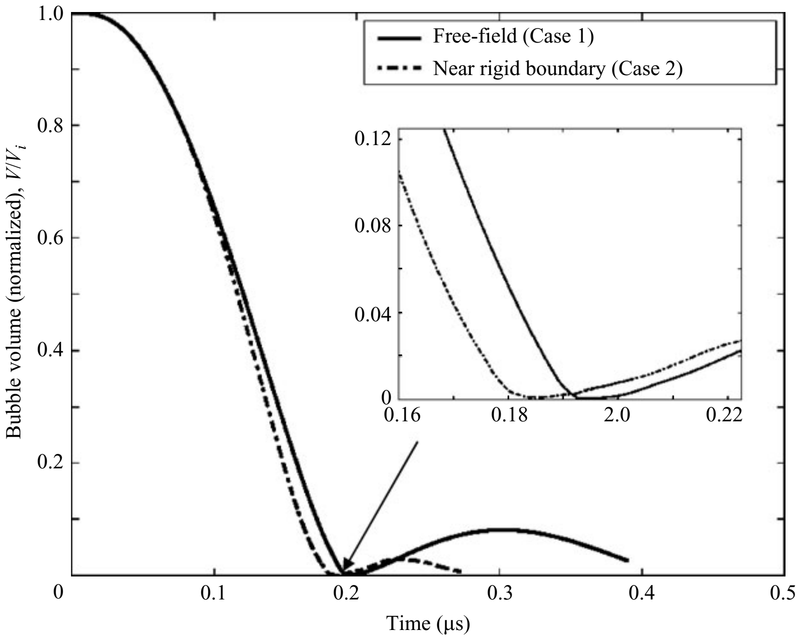

FIGURE 24. The plot of the bubble volume ratio (normalized by the initial bubble volume, V_i) with respect to time. Inset is the magnification of the point around bubble minimum volume. —, free field, case 1; ·–·, near rigid boundary, case 2.

can be run with current computational facilities. However, figure 24 does show the early stages of the expansion. It also shows that, rather than having a monotonic expansion, the bubble undergoes a micro-expansion and micro-collapse. It is clear from figure 24 that the volume attained during this first micro-expansion of the bubble, and also the time to the first micro-collapse, in case 1 are much greater that of case 2. In case 1, the remaining toroidal cavity is allowed to propagate downstream where the surrounding pressure is relatively low. This therefore allows for a larger expansion of the bubble. In case 2, the surrounding pressure remains relatively high owing to the confining effect of the boundary.

Use of the Gilmore model has for many years dominated modelling studies of the cavitation generated by lithotripsy, and indeed is responsible for the ‘gross’ impression of a monotonic expansion phase described above. Indeed, one reason for the current study was to support the design of a clinical device, the early stages of which had been based on interpretations using the Gilmore model (Leighton *et al.* 2008). An example of the way the current CFD simulations allowed new assessment of the predictions of the Gilmore model can be found in figure 25. This shows the dynamics of an air bubble of initial radius 0.04 mm in water subjected to the lithotripter pulse (figure 17) as predicted using the Gilmore model, in which the dynamics of the bubble are represented by the plot of bubble radius versus time. The assumptions of the Gilmore model are significantly different from those of the free-Lagrange code used here. Differences include the assumptions of the Gilmore model that the bubble exists in an infinite homogeneous body of fluid, the bubble remains spherical at all times, and the pressure field around the bubble is spherically symmetric (and therefore uniform over the bubble wall). As shown in the inset of figure 25, upon interacting with the lithotripter pulse, the bubble undergoes multiple micro-collapses and micro-expansions prior

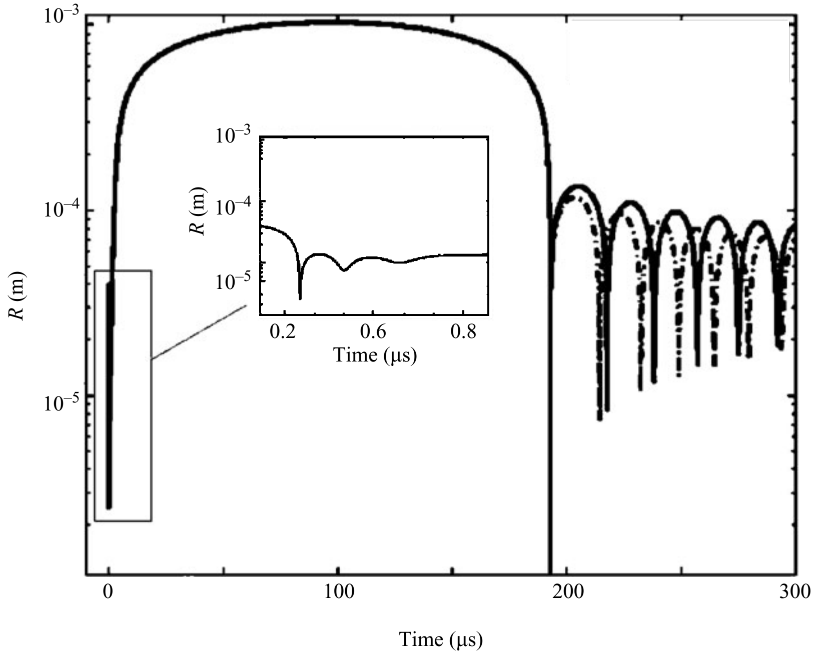

FIGURE 25. The plot of the bubble radius R versus time of the interaction of a spherical bubble (initial radius 0.04 mm) with the lithotripter pulse shown in figure 17 as predicted by the Gilmore model. The solid line and dashed line represent models with and without mass flux across the bubble interface, respectively. Inset is the magnification of the bubble initial oscillations that occur when the bubble is in the compressive regime of the lithotripter pulse.

to entering the phase of prolonged expansion caused by the tensile portion of the lithotripter pulse, followed by a second major collapse and then a series of oscillations, the amplitudes of which gradually decay as the bubble returns to a near-linear pulsation about a mean radius (Church 1989). These multiple micro-collapses and micro-expansions have not previously been reported in lithotripsy modelling.

Incompressible simulations could cover the range of the prolonged expansion before the bubble starts to have multiple collapses and rebounds (figure 25). Indeed, the coupling between the free-Lagrange simulation and that of an incompressible code (e.g. based on the boundary integral method) was originally thought by the authors to be one of potential solutions to the inability of current computational facilities to run the free-Lagrange code over the >100 μs time scales of figure 25. However, time and funding constraints prevented us from pursuing this course.

6. Conclusions

The free-Lagrange method has been shown to offer a powerful and flexible tool for the study of the dynamics of cavitation events, both two-dimensional and axisymmetric, for free-running cases where the bubble starts with expansion due to overpressure, and for lithotripter shock-induced bubble collapse applicable to studies of shock-bubble interaction in extracorporeal shock wave lithotripsy. The addition of a strength model has allowed us to visualize dynamic stress loading in adjacent solid materials of arbitrary surface profile, a facility that could be exploited in future studies of cavitation damage mechanisms. The method might also be applicable to axisymmetric liquid jet impacts of other types such as the impact of a droplet of water on a plane surface of brittle materials (Jackson & Field 2000).

C. K. T. and A. R. J. were supported through PhD studentships provided, respectively, by the University of Southampton and the EPSRC (grant no. GR/N19243; principal investigator: T. G. Leighton).

REFERENCES

Bailey, M. R., Cleveland, R. O., Colonius, T., Crum, L. A., Evan, A. P., Lingeman, J. E., McAteer, J. A., Sapozhnikov, O. A. & Williams, J. C. Jr 2003 Cavitation in shock wave lithotripsy: the critical role of bubble activity in stone breakage and kidney trauma. *Proc. 2003 Ultrasonics Symp.* pp. 724–727.

Ball, G. J. 1996 A free-Lagrange method for unsteady compressible flow: simulation of a confined cylindrical blast wave. *Shock Waves* **5**, 311–325.

Ball, G. J., Howell, B. P., Leighton, T. G. & Schofield, M. J. 2000 Shock-induced collapse of a cylindrical air cavity in water: a free-Lagrange simulation. *Shock Waves* **10**, 265–276.

Blake, J. R., Hooton, M. C., Robinson, P. B. & Tong, R. P. 1997 Collapsing cavities, toroidal bubbles and jet impact. *Phil. Trans. R. Soc. Lond.* A **355**, 537–550.

Bourne, N. K. & Field, J. E. 1991 Bubble collapse and the initiation of explosion. *Proc. R. Soc. Lond.* A *Math. Phys. Engng Sci.* **435**, 423–435.

Bourne, N. K. & Milne, A. M. 2003 The temperature of shock-collapsed cavity. *Proc. R. Soc. Lond.* A *Math. Phys. Engng Sci.* **459**, 1851–1861.

Brunton, J. H. 1967 In *Proc. Intl Conf. Rain Eros.*, 2nd (ed. A. A. Fyall & R. B. King), p. 291. Royal Aircraft Establishment, Farnborough, UK.

Church, C. C. 1989 A theoretial study of cavitation generated by an extracorporeal shock wave lithotripter. *J. Acoust. Soc. Am.* **86**, 215–227.

Coleman, A. J., Choi, M. J., Saunders, J. E. & Leighton, T. G. 1992 Acoustic emission and sonoluminescence due to cavitation at the beam focus of an electrohydraulic shock wave lithotripter. *Ultrasound Med. Biol.* **18**, 267–281.

Cunningham, K. B., Coleman, A. J., Leighton, T. G. & White, P. R. 2001 Characterising *in vivo* acoustic cavitation during lithotripsy with time-frequency methods. *Acoust. Bull.* **26**(5), 10–16.

Dear, J. P. & Field, J. E. 1988*a* High-speed photography of surface geometry effects in liquid/solid impact. *J. Appl. Phys.* **63**, 1015.

Dear, J. P. & Field, J. E. 1988*b* A study of the collapse of arrays of cavities. *J. Fluid. Mech.* **190**, 409–425.

Dear, J. P., Field, J. E. & Walton, A. J. 1988 Gas compression and jet formation in cavities collapsed by a shock wave. *Nature* **332**, 505.

Ding, Z. & Gracewski, S. M. 1996 The behaviour of a gas cavity impacted by a weak or strong shock wave. *J. Fluid Mech.* **309**, 183–209.

Field, J. E. 1991 The physics of liquid impact, shock wave interactions with cavities, and the implications to shock-wave lithotripsy. *Phys. Med. Biol.* **36**(11), 1475–1484.

Fong, S. W., Klaseboer, E., Turangan, C. K., Khoo, B. C. & Hung, K. C. 2006 Numerical anslysis of a gas bubble near bio-materials in an ultrasound field. *Ultrasound Med. Biol.* **32**, 925–942.

Hansson, I., Kendrinskii, V. & Mørch, K. A. 1982 On the dynamics of cavity clusters. *J. Phys.* D: *Appl. Phys.* **15**, 1726–1734.

Howell, B. P. & Ball, G. J. 2000 Damping of mesh-induced errors in free-Lagrange simulations of Richtmyer–Meshkov instability. *Shock Waves* **10**, 253–264.

Howell, B. P. & Ball, G. J. 2002 A free-Lagrange augmented Godunov method for the simulation of elastic–plastic solids. *J. Comput. Phys.* **175**, 128–167.

Igra, D. & Takayama, K. 1999 Investigations of aerodynamic breakup of a cylindrical water droplet. *Tech. Rep.* 11. Institute of Fluid Science, Tohoku University.

Jackson, M. J. & Field, J. E. 2000 Modelling liquid impact fracture thresholds in brittle materials. *Brit. Ceramic Trans.* **99**(1), 1–13.

JAMALUDDIN, A. R., BALL, G. J. & LEIGHTON, T. G. 2002 Free-Lagrange simulations of shock/bubble interaction in shock wave lithotripsy. *Proc. Second Intl Conf. Computational Fluid Mech.*, pp. 541–546.

KLASEBOER, E., TURANGAN, C. K., FONG, S. W., LIU, T. G., HUNG, K. C. & KHOO, B. C. 2006 Simulations of pressure-pulse bubble interaction using boundary element method. *Comput. Meth. Appl. Engng* **195**, 4287–4302.

KUWAHARA, M., IORITANI, N., KAMBE, K., ORIKASA, S. & TAKAYAMA, K. 1991 Anti-miss-shot control device for selective stone disintegration in extracorporeal shock wave lithotripsy. *Shock Waves* **1**, 145–148.

LAUTERBORN, W. 1972 High-speed photography of laser-induced breakdown in liquids. *Appl. Phys. Lett.* **21**, 27.

LEIGHTON, T. G. 2004 From seas to surgeries, from babbling brooks to baby scans: the acoustics of gas bubbles in liquids. *Intl J. Mod. Phys.* B **18**, 3267–3314.

LEIGHTON, T. G., COX, B. T. & PHELPS, A. D. 2000 The Rayleigh-like collapse of a conical bubble. *J. Acoust. Soc. Am.* **107**, 130–142.

LEIGHTON, T. G., FEDELE, F., COLEMAN, A. J., MCCARTHY, C., RYVES, S., HURRELL, A. M., DE STEFANO, A. & WHITE, P. R. 2008 A device for monitoring the efficacy of ESWL using passive acoustic emissions. *Ultrasound Med. Biol.* (submitted).

LINDAU, O. & LAUTERBORN, W. 2003 Cinematographic observation of the collapse and rebound of a laser-produced cavitation bubble near a wall. *J. Fluid Mech.* **479**, 327–348.

LUSH, P. A., TAKAYAMA, K., TOMITA, T. & OBARA, T. 1992 Cavitation and induced shock wave–bubble interaction as a cause of human tissue damage in extracorporeal shock wave lithotripsy. In *Cavitation, Proc. IMechE*, pp. 55–64.

OHL, C. D., KURZ, T., GEISLER, R., LINDAU, O. & LAUTERBORN, W. 1999 Bubble dynamics, shock waves and sonoluminescence. *Phil. Trans. R. Soc. Lond.* A **357**, 269–294.

PHILIPP, A. & LAUTERBORN, W. 1998 Cavitation erosion by single laser-produced bubbles. *J. Fluid Mech.* **361**, 75–116.

PHILIPP, A., DELIUS, M., SCHEFFCZYK, C., VOGEL, V. & LAUTERBORN, W. 1993 Interaction of lithotripter-generated shock waves with air bubbles. *J. Acoust. Soc. Am.* **93**, 2496–2509.

PLESSET, M. S. & PROSPERETTI, A. 1977 Bubble dynamics and cavitation. *Annu. Rev. Fluid Mech.* **9**, 145–185.

RAYLEIGH, LORD 1917 On the pressure developed in a liquid during the collapse of a spherical cavity. *Phil. Mag.* **34**, 94–98.

SAPOZHNIKOV, O. A., BAILEY, M. R., CRUM, L. A., MILLER, N. A., CLEVELAND, R. O., PISHCHALNIKOV, Y. A., PISHCHALNIKOVA, I. V., MCATEER, J. A., CONNORS, B. A., BLOMGREN, P. M. & EVAN, A. P. 2001 Ultrasound-guided localized detection of cavitation during lithotripsy in pig kidney in vivo. *Proc. 2001 Ultrasonics Symp.* vol. 2, 1347–1350.

SHIMA, A. 1997 Studies of bubble dynamics. *Shock Waves* **7**, 33–42.

TOMITA, Y. & SHIMA, A. 1986 Mechanisms of impulsive pressure generation and damage pit formation by bubble collapse. *J. Fluid Mech.* **169**, 535–564.

TOMITA, Y., OBARA, T., TAKAYAMA, K. & KUWAHARA, M. 1994 Cavitation phenomena in extracorporeal microexplosion lithotripsy. *Shock Waves* **3**, 149–157.

TURANGAN, C. K. 2004 Free-Lagrange simulations of cavitation bubble collapse. PhD thesis, University of Southampton, UK.

TURANGAN, C. K., ONG, G. P., KLASEBOER, E. & KHOO, B. C. 2006 Experimental and numerical study of transient bubble–elastic membrane interaction. *J. Appl. Phys.* **100**, 054910.

VOGEL, A., LAUTERBORN, W. & TIMM, R. 1989 Optical and acoustic investigations of the dynamics of laser-produced cavitation bubbles near a solid boundary. *J. Fluid Mech.* **206**, 299–338.

VYAS, B. & PREECE, C. M. 1976 Stress produced in a solid by cavitation. *J. Appl. Phys.* **47**, 5133–5138.

WILKINS, M. L. 1999 In *Computer Simulation of Dynamic Phenomena*, pp. 128–167. Springer.

ZEMAN, R. K., DAVROS, W. J., GOLDBERG, J. A., GARRA, B. S., HAYES, W. S., CATTAU, E. L., HORII, S. C., COOPER, C. J. & SILVERMAN, P. M. 1990 Cavitation effects during lithotripsy. Part II. Clinical observations. *Radiology* **177**, 163–166.